Harnessing Atomic Layer Deposition and Diffusion to Spatially Localize Rare-Earth Ion Emitters

Alban Ferrier, Nao Harada, Marion Scarafagio, Emrick Briand, Jean-Jacques Ganem, Ian Vickridge, Antoine Seyeux, Philippe Marcus, Diana Serrano, Philippe Goldner, et al.

C: Plasmonics; Optical, Magnetic, and Hybrid Materials

Harnessing Atomic Layer Deposition and Diffusion to Spatially Localize Rare-Earth Ion Emitters

Alban Ferrier, Nao Harada, Marion Scarafagio, Emrick Briand, jean-jacques Ganem, Ian Vickridge, Antoine Seyeux, Philippe Marcus, Diana Serrano, Philippe Goldner, and Alexandre Tallaire

J. Phys. Chem. C, **Just Accepted Manuscript** • DOI: 10.1021/acs.jpcc.0c04019 • Publication Date (Web): 18 Aug 2020

Harnessing atomic layer deposition and diffusion to spatially localize rare-earth ion emitters

Alban Ferrier[1,2], Nao Harada[1] , Marion Scarafagio[1], Emrick Briand[3], Jean-Jacques Ganem[3], Ian Vickridge[3], Antoine Seyeux[1], Philippe Marcus[1], Diana Serrano[1], Philippe Goldner[1] and Alexandre Tallaire[1]*

[1] Institut de Recherche de Chimie Paris (IRCP), Université PSL, Chimie ParisTech, CNRS, 75005 Paris, France

[2] Sorbonne Université, Faculté des Sciences et Ingénierie, UFR 933, 75005 Paris, France

[3] Sorbonne Universités, Institut des NanoSciences de Paris, INSP, 75005 Paris, France

KEYWORDS : Spatial localization of emitters, Atomic Layer Deposition (ALD), Europium diffusion, hole burning spectroscopy, Quantum Technologies

*corresponding author: alban.ferrier@chimieparistech.psl.eu

ABSTRACT: Control of rare-earth ions doping profiles is a key challenge for several photonics applications and for quantum technologies that require spatially localized emitters. In this work, we propose to use Atomic Layer Deposition (ALD) followed by an annealing post treatment to localize europium emitters close to the surface of an Y_2O_3 film or an Y_2SiO_5 single crystal by exploiting in-diffusion. Indeed, ALD is a conformal method that can provide in-depth nanometer-scale positioning accuracy on a large scale. However, the post thermal annealing required to achieve higher crystalline quality and to activate diffusion, needs to be precisely controlled to maximize our ability to localize ions. In this paper, we evaluate europium ion diffusion in an ALD-grown $Eu_2O_3/Y_2O_3/Si$ stack using Rutherford Backscattering Spectroscopy (RBS) and Time of Flight Secondary Ion Mass Spectrometry (TOF SIMS). We then extend this approach to investigate diffusion from an Eu_2O_3 ALD film into a single crystalline substrate of Y_2SiO_5 (YSO), a technologically relevant material system for quantum applications. We determine Eu^{3+} diffusion coefficients in both cases and show that in the polycrystalline Y_2O_3 ALD sub-micron film, diffusion starts at 950 °C whereas in single crystal YSO it becomes significant, only above 1200 °C. Finally, spectral hole burning of such in-diffused emitters revealed homogeneous lines as narrow as 2 MHz. This study indicates that an appropriate annealing of ALD-grown rare-earth oxide films can

be harnessed to create localized dopants that preserve their outstanding optical properties, a pre-requisite for their integration into photonic and quantum devices.

1. Introduction

Lanthanide doped oxide crystalline hosts are well known luminescent platforms for photonic applications. Indeed their unique optical properties have advanced a broad range of applications including lighting, sensors, bio-imaging or more recently Quantum Technologies (QT).[1] The development of rare-earth (RE) doped films[2–8] presents several benefits as compared to bulk single crystals. For example, the use of waveguides or multilayer architectures can increase the light matter interaction and thus device operation and sensitivity. In addition, the spatial localization of RE ions closed to the surface is highly desirable for exploiting their coherent properties within a quantum device, in particular for improved coupling to a cavity or to an hybrid structure.[9,10,11,12] For example in several quantum sensing schemes, the sensitivity scales as the square root of the number of interacting emitters while coupling to the external field to be sensed can be maximized by placing the emitters close to the surface (10s of nanometer).[13] High emitter concentration closed to the surface is required, whereas emitters inside the bulk will decrease the sensitivity since they are insensitive to the surface perturbation. This closed to surface doping is

not accessible with classical bulk crystal growth where the dopant is inserted in the melt and is distributed according to the segregation law. Finally, lanthanide dopant concentration profiles along the film might also be of interest for optimized up-conversion or lighting.[14]

Currently, the most common technique for ion localization is ion implantation. Indeed, ion implantation is a powerful approach to precisely localize atoms within a crystalline matrix at controlled depths.[15] However, implantation induces damage and defects especially when heavy atoms (like lanthanides) are considered.[16] This defects contribute to increase the spectral broadening of the emitters and reduces the overall performance (e.g. larger homogeneous and inhomogeneous linewidth, lower quantum efficiency). [17,18] Furthermore the implantation yield is typically less than 50 %, indicating that at least half of the implanted ions do not emit photons. This low yield can be very detrimental for QT since decoherence rates are in general related to the coupling with other spins of the matrix (e.g. in particular other implanted yet inactive ions). For instance, to our knowledge, no Spectral Hole Burning (SHB) has been demonstrated on lanthanide-implanted single crystals. However, SHB is a key requirement in QT for the quantum states initialization by allowing spectral tailoring of the inhomogeneous absorption profile by efficient population transfer between ground-state hyperfine levels using optical pumping.[1]

Therefore, other strategies that preserve ion properties while allowing high localization efficiency are desirable.

Atomic Layer Deposition (ALD) is highly suited for precisely controlling the composition and nanoscale in-depth positioning of dopants in a thin film. Indeed, the sequential injection of precursors enables a slow layer-by-layer growth mode with a high flexibility. It offers large wafer-scale process-ability as well as deposition on complex nanostructures. The use of appropriate ligands with large steric hindrance can increase the distance between RE ions in the lateral direction thus improving in-plane positioning as well. [14,19,20] Recently, we demonstrated for ALD-grown Eu^{3+}-doped Y_2O_3 thin films using $Y(tmhd)_3$ and ozone as precursors that a high deposition temperature (350 °C) and post treatment annealing above 900°C are key parameters for optimizing the luminescent properties.[21] In fact, by improving the crystalline environment of the ions, inhomogeneous lines of 200 GHz were obtained for the $^7F_0 \rightarrow {}^5D_0$ transition of Eu^{3+} even for nanoscale films (thickness < 100 nm) which is a promising first step towards their integration in QTs. One obvious drawback of this approach is related to the fact that at such a high annealing temperature, RE dopants are mobile and can interact at the interface with silicon. Too high annealing temperature is so detrimental since it will lead to modification of the spatial distribution of RE ions, as well as formation of a silicate phase at the interface.[21] These are detrimental to the

precise positioning of emitters as well as the control of their environment. Phase mixing indeed affects the frequency range of ions' emission, leads to strong inhomogeneous broadening and increases the dephasing processes rate by disorder mode.[22,23]

Diffusion of lanthanide ions in single crystals or ceramics like Al_2O_3, $Y_3Al_5O_{12}$ or YVO_4 has been reported for a large range of applications including mineralogy, waveguide fabrication or ceramic sintering. [24,25,26,27,28] For photonics, thermal diffusion of transition metals has been extensively studied to form low cost waveguides in $LiNbO_3$.[29] In that case, the transition metal ion acts as a local refractive index modifier leading to passive waveguides. Further works have demonstrated that thermal diffusion is also a useful approach for RE doping in oxide single crystals for laser applications.[11] However, only scarce data exists on diffusion in nanometer-scale films obtained by ALD or more generally about ions' redistribution during thermal annealing.[30] Annealing temperature and duration need to be carefully optimized in order to preserve dopant localization or to harness their diffusion, as well as to avoid unwanted phases formation.

In this study, we focus on the diffusion of Eu^{3+} cations during thermal annealing using Rutherford Backscattering Spectroscopy (RBS) and Time of Flight Secondary Ion Mass Spectrometry (TOF SIMS). We first study Eu^{3+} diffusion in an ALD-grown Eu_2O_3/Y_2O_3/Si (100) stack in the 600-

1000 °C range (Fig. 1a) from which we determine the diffusion coefficient as well as investigate the reactivity at the interface. This multilayer presents the advantage of being directly grown by ALD on a standard low cost and large area Si wafer but possesses limited crystallinity. We then extend this study to Eu^{3+} diffusion from an ALD-grown Eu_2O_3 layer above a bulk Y_2SiO_5 (YSO) single crystalline substrate grown by Czochralski (Fig. 1b) which is the most common host crystal used for RE based QTs.[1] In this latter case, we demonstrate that diffusion at higher temperatures (1000-1500 °C) can be explored as an alternative to ion implantation in order to create localized RE ions close to the YSO surface, within the first 200 nm. We observe SHB from such in-diffused ions and measure a promising hole linewidth of 4 MHz. This indicates that this strategy is suitable to engineer materials that could provide a suitable platform for QTs.

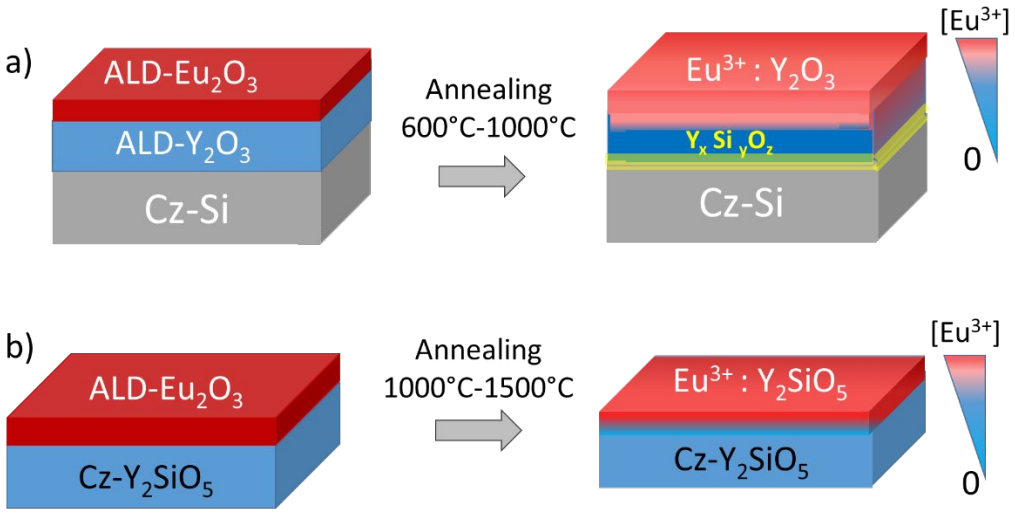

Figure 1: Schematic representation of the two sets of samples investigated. a) Diffusion of Eu^{3+} from a Eu_2O_3 layer (typically 15 to 20 nm thick) on Y_2O_3 (120 nm thick). The two layers were deposited by ALD on Czochralski silicon (Cz-Si) wafer (100). b) Diffusion of Eu^{3+} from a Eu_2O_3 layer (20 nm thick) deposited on a thick b-oriented single crystalline YSO substrate (010) grown by Czochralski method (Cz) and optically polished.

2. Method

Eu_2O_3 and Y_2O_3 film depositions were carried out by ALD with a *Picosun Sunale R200* using conventional β-diketonate precursors: $Eu(tmhd)_3$ and $Y(tmhd)_3$ (99.9 % purity from *Strem Chemicals*). The precursors were held at 160°C and delivered using 300 sccm N_2 as a carrier gas. Ozone (O_3) was used as a strong oxidizing agent. The precursors were flown sequentially with 3 s injection time into the thermalized deposition chamber at 350 °C. The number of cycles was adjusted in order to obtain the desired thickness. More details about the impact of the different deposition parameters and their optimization are discussed in a previous study.[21] For the $Eu_2O_3/Y_2O_3/Si$ stack, a first 120 nm-thick Y_2O_3 layer was grown on a Si (100) wafer covered by a native oxide (SiO_2). Pre-annealing of the cubic Y_2O_3 layer at 900 °C for 2h under air was carried out prior to the growth of 15 nm thick Eu_2O_3 (see Fig. 1a). [31,32] After this pre-annealing yttria films

remain polycrystalline with strong texturation along (100).[21] For the second deposition, a slight thickness variation of the Eu_2O_3 layer is observed from sample to sample. This thickness variation is possibly due to slightly varying growth conditions and positioning inside the reactor chamber but it does not notably change the diffusion profile.

For the Eu_2O_3/Y_2SiO_5 stack, a 20 nm-thick layer was directly deposited by ALD on a specially prepared single crystalline substrate (see Fig. 1b). Monoclinic YSO was grown by Czochralski method (Cz) along the b direction following the procedure described by Ferrier et al. [33,34] After crystal orientation by the Laue method, it was cut and optically polished perpendicularly to the b direction.

Film thickness was estimated by white light interferometry in the range 250-1000 nm with an *Ocean Optics NanoCalc* and an *ISE Woollam* spectroscopic ellipsometer system. Eu_2O_3 and Y_2O_3 optical constants have been fitted using a Cauchy model. Thermal annealing was performed in air in the range 600-1500 °C for 2 h in order to activate europium diffusion from the top layer into the layer beneath.

RBS and TOF-SIMS bring complementary information and are both explored here to assess Eu^{3+} diffusion mechanisms. Indeed, RBS is non-destructive and provides quantitative atomic

composition with a 10 nm in-depth resolution whereas TOF SIMS is used to determine with high accuracy (less than 1 nm) the depth profiling of different elements as already demonstrated for ALD deposited layer on metallic substrates.[35–38]

Ion beam analyses (RBS and NRA) were carried out using the Van de Graaf accelerator of the SAFIR Platform of Sorbonne Université. RBS was performed with 1800 keV $^{4}He^{+}$ beam in a non-channeling geometry. In RBS, the energy of the backscattered ions depends on both the element with which the ion experienced an elastic collision as well as its depth positioning within the target material. In addition, the area of the peak related to an element is proportional to the atomic density of this element in the material. To determine the concentration profile, a simulation was carried out using the SIMNRA software (more details available on Supplementary Materials).[39] As we used a silicon substrate, the precise determination of elements lighter than silicon by RBS is complicated. That's why for $Eu_2O_3/Y_2O_3/Si$, the oxygen areal densities were also determined by nuclear reaction analysis (NRA) using the $^{16}O(d,p)^{12}C$ reaction induced by a deuteron beam of 850 keV and a detection angle of 150°. Indeed, this nuclear reaction is specific to oxygen allowing quantification by a simple integration of the proton peaks on the NRA spectrum (see Figure S1). Then, comparison of those integrated values with two standards of Ta_2O_5 allowed precise

determination of the oxygen composition of the thin film. Good agreement was obtained between the O content extracted from RBS and NRA studies with typical variation of about 2%.

The in-depth concentration profiles were also studied using a dual-beam TOF-SIMS V spectrometer (*ION-TOF GmbH, Muenster, Germany*). Indeed, we measured the concentration depth profile of the yttrium and erbium ions at a sufficiently low primary ion dose density to keep static conditions. Charge compensation was performed by using an electron flood gun. The spectrometer was operated at a pressure of 10^{-9} mbar. A pulsed 25 kV Bi^+ primary ion beam delivering 1 pA over a 100×100 μm² area is used to extract the chemical species from the surface. The masses of the removed chemical species are determined by time-of-flight mass spectroscopy. The sputtering of the surface was done using a 2 keV Cs^+ sputter gun giving a 100 nA target current over a 300×300 μm² area. The interlacing between Bi^+ and Cs^+ guns allows to record TOF-SIMS depth profiles. Analysis was centered inside the sputtered crater to avoid edge effects. Data acquisition and post-processing were carried out using *Surface Lab 6.7* software. The sputter profiles were converted into depth by measuring the crater's depth with a surface profiler (*Dektak 150, Veeco*), assuming a constant sputtering rate. The main uncertainty of this data results from the limited accuracy of the depth scaling. TOF-SIMS is destructive but is well adapted to determine dopant concentration profiles being done with accuracy better than 1 nm.

Furthermore, TOF-SIMS requires precisely calibrated standards and is function of the analyzed matrix for quantitative assessment since the ionization yield of each element is generally different, Eu and Y contributions were assessed by following EuO_2^- and YO^- sputtered ions signals. Contribution from other elements (SiO^-, C and Si) were also analyzed but will not be discussed in detail in this paper. In particular, the precise determination of the top layer's thickness was difficult due to the roughness induced by the annealing post treatment.

Finally, SHB experiments were performed with a homemade low temperature microscope using a high numerical aperture lens on a nano-positionner (See Supplementary Materials for more details and Figure S4). Briefly, samples were introduced into a He bath cryostat (*Janis SVT-200*). The temperature was monitored directly on the sample-holder by a Si diode (*Lakeshore DT-670*). A continuous wave (CW) dye laser (*Sirah Matisse DS*) with 300 kHz linewidth provided the optical excitation around 580 nm. Pulsed sequences required for SHB measurements were created by modulating the CW laser with one acousto-optic modulator driven by an arbitrary waveform generator (*Agilent N8242A*). The red luminescence was filtered using band-pass and interferential filters and sent to a high sensitivity photomultiplier (*PMT R10699 Thorlabs*).

3. Results and discussion

3.1. Eu^{3+}diffusion in an ALD-grown Eu_2O_3/Y_2O_3/Si (100) stack

We first focus on reactions occurring at the substrate/layer interface of the ALD-grown polycrystalline Eu_2O_3/Y_2O_3/Si (100) stack during thermal annealing. Typical RBS spectra for 2 different annealing temperatures are presented in Fig. 2. The contribution from silicon, oxygen, yttrium and europium are clearly visible. No additional elements appear on the RBS spectrum indicating no obvious contamination with elements heavier than silicon. Carbon was found to be below the detection limit of RBS. However, the detection of elements lighter than the substrate is always challenging in RBS since their signals are superimposed to that from the substrate. NRA was thus used to quantify oxygen and check the carbon content (Figure S1). The evolution of the composition assessed from the integration of the RBS and NRA signals is illustrated in Table 1. For the as-grown film, the RE to oxygen ratio is close to the expected stoichiometric value (0.4) but with a slight excess of oxygen. This excess is likely due to the diffusion of oxygen inside the sesquioxide structure during the annealing under air. Another source of oxygen over-stoichiometry is the formation of silicate parasitic phases at the silicon interface during the pre-annealing of the Y_2O_3/Si template prior to Eu_2O_3 deposition. Using SIMNRA software fitting, we evaluate a SiO_2 layer of 30 nm for a 900°C annealing post treatment, in reasonably good agreement with the 22 nm determined by spectroscopic ellipsometry (Figure S2). When the

annealing temperature of the multilayer is increased above 900 °C, interfacial reactions take place again leading to a further increase of the oxygen over-stoichiometry (see Table 1 and Figure S2). An increase of the SiO_2 interlayer's thickness was evidenced by spectroscopic ellipsometry measurements (Figure S2) and is reported in the last column of Table 1. The silicon oxidation is also clearly evidenced on the RBS spectra of Fig. 2c where a shoulder at the silicon front edge appears, indicating the formation of an oxide interlayer. Annealing at temperatures higher than 1000 °C could not be carried out since the reaction between the layer and the substrate leads to a depletion of the 120 nm-thick yttria layer into orthosilicate and/or pyrosilicate phases, which are not desirable.[21,40] This indeed sets the upper temperature limit for annealing such multilayers if one wants to keep a constant crystalline environment for the ions.

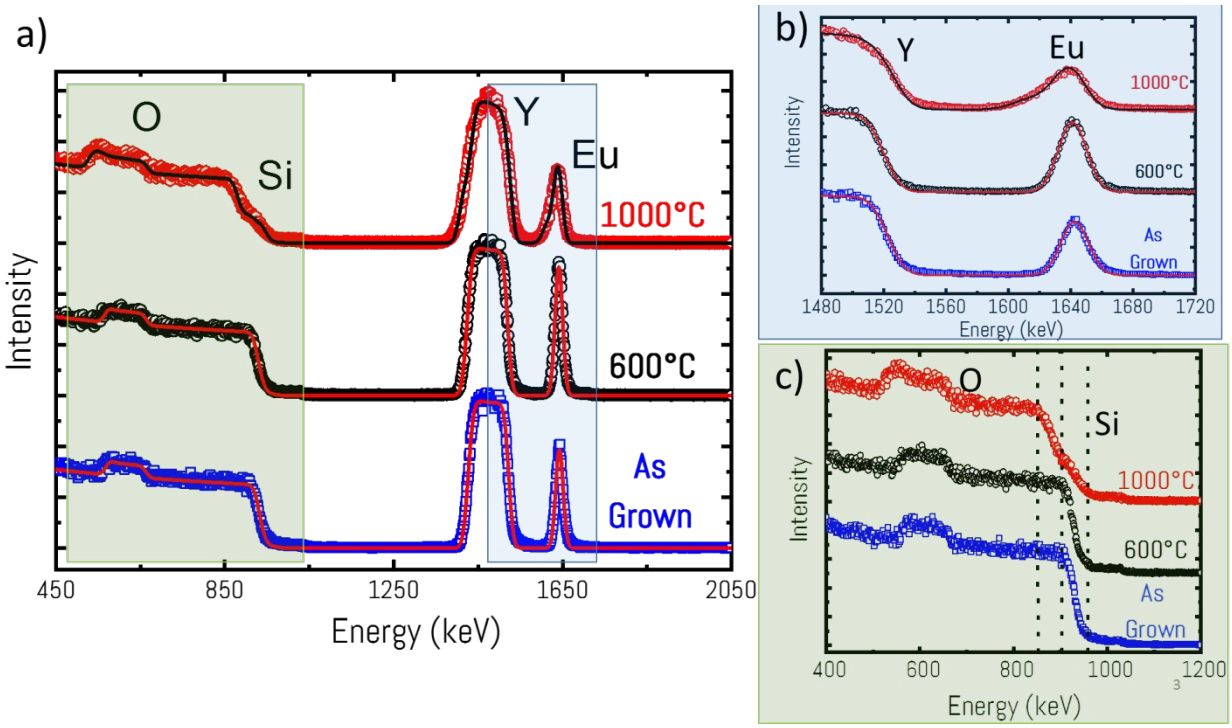

Figure 2 (a) RBS spectra of a Eu_2O_3/Y_2O_3/Si stack either as-grown or annealed at 600 or 1000 °C for 2 hours. (b) Zoom into the region highlighted in blue. Experimental data are dots points whereas SIMNRA simulation is presented with solid lines. (c) Zoom into the region highlighted in green. Data are vertically translated for better clarity.

Table 1 : RBS and NRA quantification data. The SiO_2 thickness estimated from ellipsometry is also presented. The oxygen content used for the determination of the integrated stoichiometry

*was determined by subtracting the oxygen content in the parasitic interfacial layers determined by the RBS simulation to the total content of oxygen. A good agreement between the thickness of the SiO_2 layer determined by the RBS simulation and ellipsometry is observed (see also Figure S2). The expected stoichiometry is 0.4. * Note that for the as-grown layer, pre-annealing of the Y_2O_3 layer at 900 °C for 2h was carried out prior to Eu_2O_3 deposition.*

Samples	Y RBS (10^{15} at/cm^2)	Eu RBS (10^{15} at/cm^2)	O NRA (10^{15} at/cm^2)	Stoichiometry ∫(Y+Eu)/∫(Y+Eu+O*)	SiO_2 thickness ellipsometry (nm)
As grown*	301	20	670	0.35	22
600 °C / 2 h	301	24	690	0.35	24
800 °C / 2 h	301	15	702	0.35	28
900 °C / 2 h	296	14	836	0.35	52
950 °C / 2 h	298	24	1071	0.34	107
1000 °C / 2 h	307	21	1081	0.34	118

We then evaluate europium diffusion into the yttrium oxide layer beneath. yttrium and europium have the same valence state (3+) and similar ionic radii (4 % difference) that lead to possible inter-diffusion when heated.[41] RBS spectra of Figure 2a were fitted using the SIMNRA software. The staircase-shape Eu^{3+} depth profile that was used to get a good fit is presented in Figure 3 for different annealing temperatures (see also Figure S3). We observe that the Eu^{3+} distribution starts to change only for temperatures above 900°C with significant Eu^{3+} and Y^{3+} inter-diffusion at 950°C. This large temperature of inter-diffusion is due to the refractory character of Y_2O_3 and Eu_2O_3 with melting temperatures of about 2400°C. We note though that the considered films are polycrystalline and that higher diffusion is expected than in single crystal materials due to the presence of grain boundaries. For the 1000°C case, the RBS composition indicates that the europium concentration starts to be depleted at the surface. The concentration distribution after a diffusion anneal is described by the thin film diffusion solution.[42] Therefore, we fit the curve with the diffusion Gaussian function such as :[42]

$$C(z,t) = A * exp^{-\left(\frac{z^2}{4Dt}\right)} \; with \; A = \frac{\tau C_0}{\sqrt{\pi D t}} \quad \text{(eq. 1.)}$$

where τ is the initial film thickness of Eu_2O_3, C_0 is the maximum solid solubility of Eu^{3+} in Y_2O_3. Using this equation, we were able to simulate the staircase profile considered in our RBS fit (see

purple and red square curves of Fig. 3) and to extract a diffusion coefficient of 4.5×10^{-21} and 2×10^{-20} $m^2.s^{-1}$ at 950°C and 1000 °C respectively. However, a relatively large uncertainty is expected due mainly to the low accuracy in depth resolution of RBS and the surface roughness. In order to obtain more precisely the diffusion coefficient, TOF-SIMS analyses were performed.

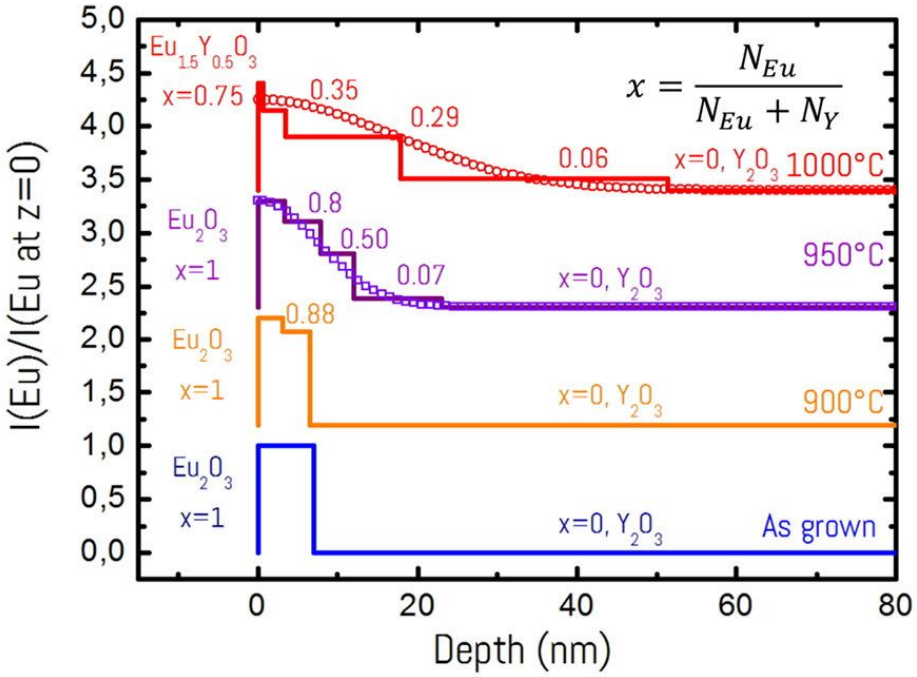

Figure 3. Comparison of diffusion depth profiles of Eu in the Eu_2O_3/Y_2O_3/Si stack for different annealing temperatures. The solid lines correspond to the staircase Eu *distribution used in the SIMNRA simulation of the RBS spectra. For the two highest temperatures, we simulate the diffusion with the Gaussian function distribution using Eq. 1 (dots and square points). The depth (z) has been determined assuming a density of 5.3 g cm^{-3} and 7.02 g cm^{-3} for Y_2O_3 and Eu_2O_3*

respectively. The cationic composition has been indicated for each sublayer using the ratio x where $x = N_{Eu}/(N_{Eu}+N_Y)$*. The data have been vertically shifted and normalized to the Eu content value at the surface (z=0) for clarity.*

The main advantage of TOF-SIMS is the sub-nm depth resolution in comparison to the few nm resolution of RBS. The depth profiles of Eu, Y, Si, C and O in the as-grown thin layers are presented in Fig. 4. Carbon contamination is clearly detected which is expected to originate mainly from the surface and possibly from the long carbon chains of the ALD precursors. The TOF SIMS spectra demonstrated a chemically stable and well-defined interface between Eu_2O_3, Y_2O_3 and Si for the as-grown layers from the abrupt changes and little overlapping of the signals. Eu ions appear to be located within the top 15 nm. When the sample is annealed at high temperature, the Eu signal spread out over up to 60 nm (Fig. 4b and 4c) confirming diffusion. A good agreement is observed between the Eu staircases deduced from RBS with the Eu profile element measured by TOF-SIMS (Figure S3). Using the same equation as before (Eq. 1), we were able to estimate the diffusion coefficients to 4×10^{-21} and 1.8×10^{-20} $m^2.s^{-1}$ at 950°C and 1000 °C respectively. The diffusion coefficient plotted in Fig. 5 together with those estimated by RBS indeed agree fairly well.

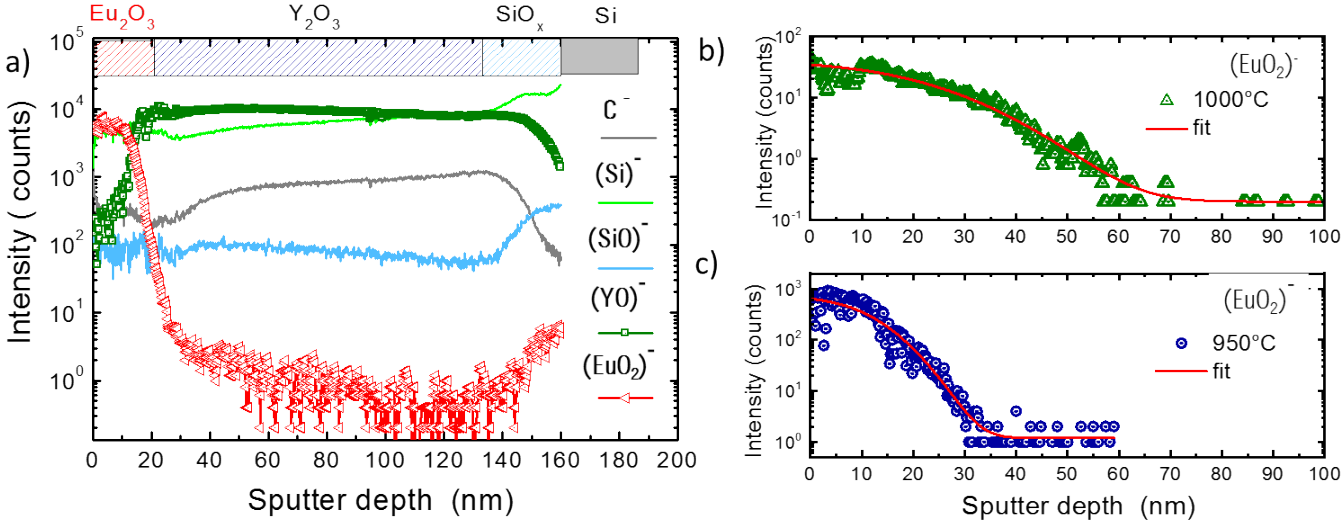

Figure. 4: TOF-SIMS analysis of a thin Eu_2O_3/Y_2O_3/Si stack. (a) Before annealing from which the different layers can be clearly identified. (b) and (c) Profiles of the Eu element for annealing at 1000 °C and 950°C for 2h respectively. Dots are experimental results while solid lines are modelling using diffusion equations (1).

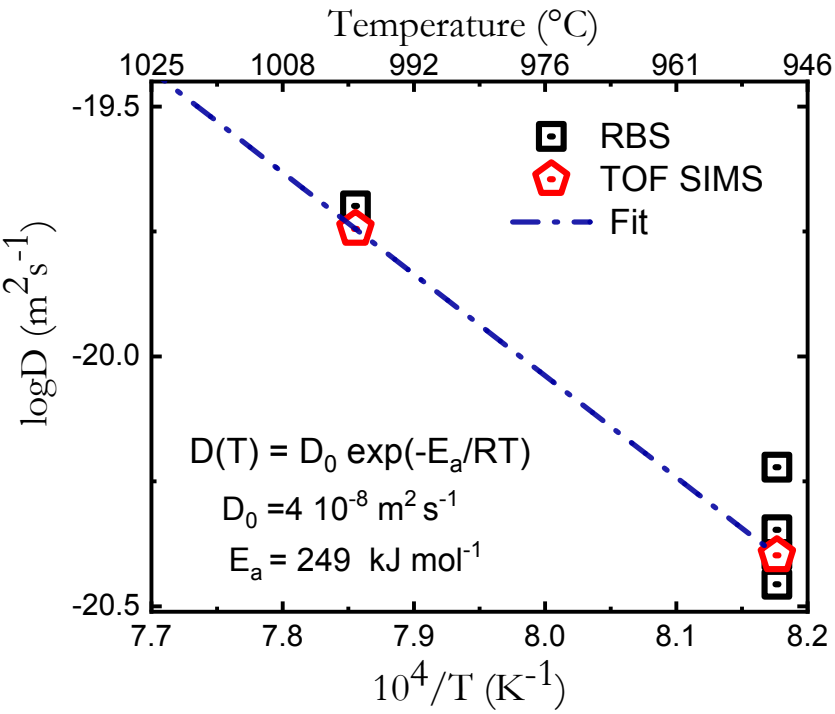

Figure 5: Europium's diffusion coefficient as a function of the reciprocal of the absolute annealing temperature (Arrhenius plot) from TOF SIMS and RBS. Symbols are experimental points and solid line is the fit using an Arrhenius law. For 950°C annealing post-treatment, measurements have been performed for different durations. Arrhenius parameters extracted from the fit are presented in the figure.

From those measurements, we deduced the activation energy according to the well-known Arrhenius equation:

$$D(T) = D_0 e^{-\left(\frac{E_a}{RT}\right)} \quad \text{(eq. 2)}$$

where D_0 is a prefactor, E_a is the activation energy and T the temperature. The activation energy is about 249 kJ mol^{-1} for both RBS and SIMS data. As only two temperatures have been considered, this calculation has limited validity. Nevertheless, those E_a values are close to those of self-diffusion reported for yttrium in the literature that are comprised between 246 and 320 kJ mol^{-1} for higher temperature treatments in a Y_2O_3 single crystal.[43]

In summary, Eu^{3+}-diffusion into a polycrystalline ALD film of Y_2O_3 occurs significantly only for temperatures above 900 °C, while the formation of an interfacial oxide phase on silicon remains limited in the 900°C-1000°C annealing temperature range. This indicates that post-deposition thermal treatment at moderate temperatures can be harnessed to improve the luminescent properties of ALD-grown films without affecting the in-depth spatial localization of RE ions. This approach opens the way to the fabrication of complex planar multilayer structures in order to increase the photoluminescence or to manage energy transfer using the same strategies than that used with multi core-shell doping in up-conversion nanocrystals.[44–46] We then extended this approach to the context of QTs where localized emitters closed to the surface are especially desirable. For that purpose, we probed Eu^{3+} ion diffusion into quantum-grade quality Y_2SiO_5 single crystals since YSO has already been used in some of the most advanced demonstrations in QTs.[47–49]

3.2. Eu^{3+} diffusion in Y_2SiO_5 single crystals

A 20 nm-thick Eu_2O_3 ALD film was deposited on undoped Y_2SiO_5 single crystal substrates that were cut perpendicular to the *b* axis and optically polished (Fig. 1b). Different annealing temperatures and duration times, as shown in Table 2, were used to activate diffusion from the Eu^{3+} containing layer into the crystal. Analysis was carried out by a combination of TOF-SIMS and RBS. In the RBS spectra of Figure 6, the calculated Eu^{3+} atomic density from the integration of the peak appears constant and independent of the thermal post-treatment (see Table S1) indicating that Eu^{3+} loss does not occur. However, with annealing at temperatures above 1200 °C, the RBS Eu^{3+}-related peak became asymmetric on the low energy side (i.e. at greater depths) confirming Eu^{3+} diffusion into the YSO substrate. Moreover, a Y out-diffusion into the film is also observed since the Y-related contribution of the substrate becomes modified on the high-energy side (i.e. indicating Y atoms are located closer to the surface). Apart from this, no modification of the substrate was observed even for the highest annealing temperatures. This is a clear advantage of this approach as compared to the previously considered thin ALD multilayer stack where the formation of an interlayer oxide with the substrate limits the maximum annealing temperature. To evaluate diffusion from the film, we performed simulation of the RBS spectra with SIMNRA multilayer. However due to the low depth resolution and the overlapping of the 2 main

peaks (Y and Eu) a precise value of the diffusion coefficient could not be extracted. We thus turned to TOF-SIMS that can provide more accurate depth analysis.

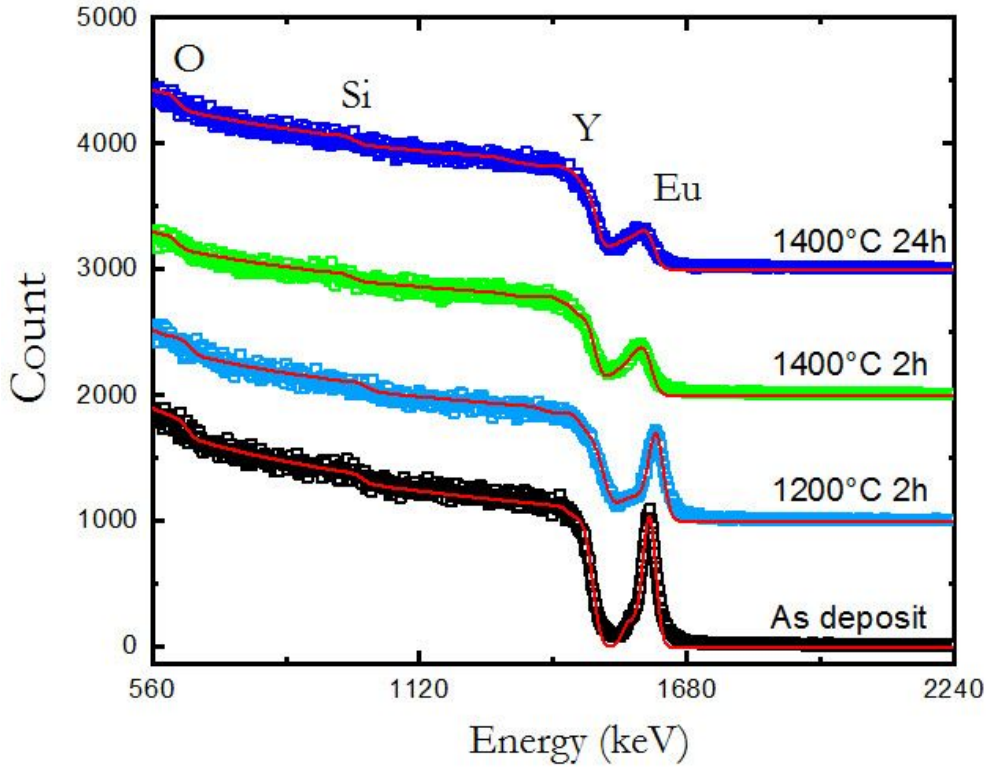

*Figure 6: RBS spectra showing europium diffusion from a Eu_2O_3 ALD layer into a Y_2SiO_5 single crystal substrate as a function of the annealing treatment. Square points are experimental data whereas solid lines represent simulation with the SIMNRA software. For all curves, a similar content of Europium has been deduced from the simulation (*see Table S1*). The curves have been translated vertically for better clarity.*

Typical experimental curves relative to Eu and Y contributions in TOF-SIMS are presented in Fig. 7. For the as-grown ALD film, an abrupt decrease of the EuO_2^- signal indicates a well-defined interface between the 20 nm-thick Eu_2O_3 film and the YSO substrate. When the annealing temperature is increased up to 1400 °C, diffusion of Eu ions into YSO occurs as shown from the spreading of the EuO_2^- signal (Fig. 7a). Similarly, diffusion of yttrium ions from the substrate into the ALD layer is also visible from the shape of the YO^- signal in Fig. 7b. When looking in more details at the Eu-related contribution, one can note that for short annealing, the semi-logarithmic plot indicates a two-component concentration profile of Eu inside YSO, which is far less observed for the long 1400°C annealing (see Fig. 8a and 8b). In the latter case, Eu^{3+} distribution can be well fitted by a Gaussian distribution (Equation 1). Two-component diffusion profiles have already been observed in polycrystalline materials such as ceramics and have been classified by Harrison in three different kinetics regimes called A, B and C.[42,50] These different regimes exist due to the presence of several diffusion paths with different coefficients. Indeed, the diffusion coefficient inside the bulk material is significantly smaller than at the grain boundary for polycrystalline materials or for diffusion at dislocations in single crystals. For the A regime the bulk diffusion and the faster diffusion process are averaged and only an effective diffusion D_{eff} coefficient is observed. This A kinetics is observed for high temperature or longer annealing times and a

Gaussian diffusion profile is expected for depleted source. For B regime, the diffusion profile presents two different slopes. The first slope of the profile corresponds to the effective diffusion D_{eff} across the bulk materials whereas the second part of the profile, i.e. the curved tail, is characteristic of the diffusion along the fast path (grain boundaries, dislocation etc…).[42] Indeed, thermal diffusion of ions in single crystals has revealed that large tails in the concentration profile can be created as a consequence of the existence of dislocations that act as "short circuits" for the thermally diffused ions, leading to unusual large penetration.[51] The C kinetics corresponds to condition where the bulk diffusion is extremely low and is not in agreement with our experimental conditions. According to Harrison model only one diffusion is expected in single crystal but the B regime has already been observed in several materials.[51,52] Possible explanations are the existence of dislocations or of large anisotropy cationic diffusion with the direction as already observed for other oxide.[25,52] The latter effect should be important in our crystal since YSO is monoclinic. Indeed, for YSO the diffusion parameter is described with a second rank symmetric tensor with 4 independent parameters. More studies are required in order to fully characterize this process.

The diffusion coefficients extracted from the Gaussian distribution for different temperatures or annealing durations are presented in Table 2. As expected, an increase of the diffusion

coefficients is observed with the annealing temperature. Indeed, the effective diffusion coefficient is estimated to 2×10^{-21} and 5×10^{-20} $m^2.s^{-1}$ at 1200 and 1400 °C respectively. The obtained diffusion coefficients of Eu^{3+} in YSO are small and of the same order of magnitude than lanthanides in other refractory oxides (such as YVO_4 and YAG) that are shown for comparison in Table 2. Eu diffusivity in YSO appears similar to that observed for other lanthanides. The diffusion of different trivalent lanthanides can be compared since lanthanide diffusion exhibits only a weak dependence on ionic radius for various minerals, both silicates and non-silicates. [53]

Finally, the calculated diffusion coefficients were plotted in Fig. 9 as a function of temperature. The activation energy of Eu^{3+} in YSO was estimated to 260 $kJ.mol^{-1}$. This value is in the characteristic range for lanthanides in oxide single crystals. [27]

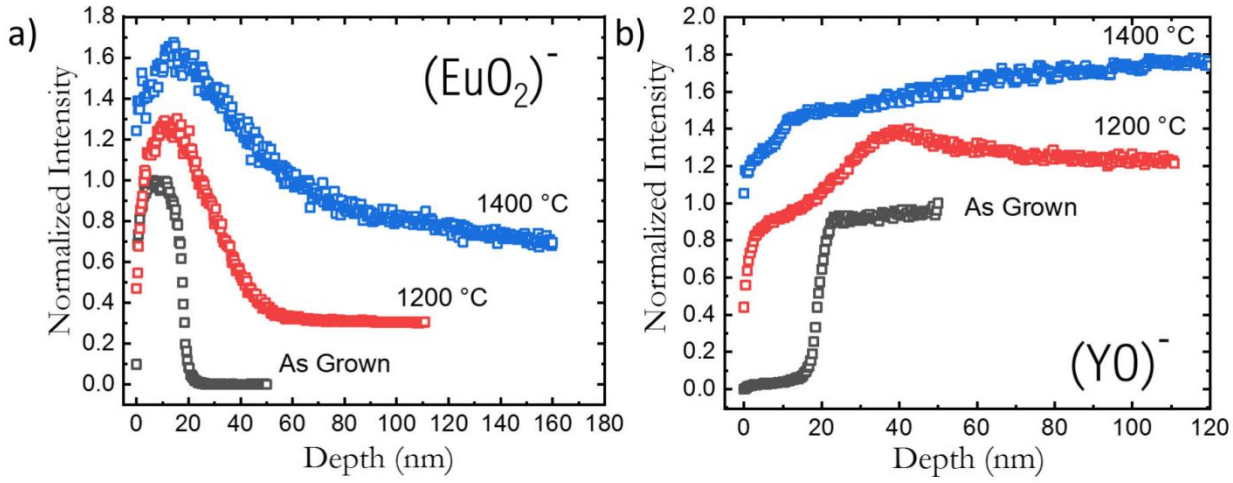

Figure 7: TOF-SIMS analysis of a thin ALD-grown Eu_2O_3 thin film on Y_2SiO_5 showing the Eu and Y related signals at different annealing temperatures. Annealing duration was 2h. The curves have been normalized to their maximum and vertically translated for better clarity.

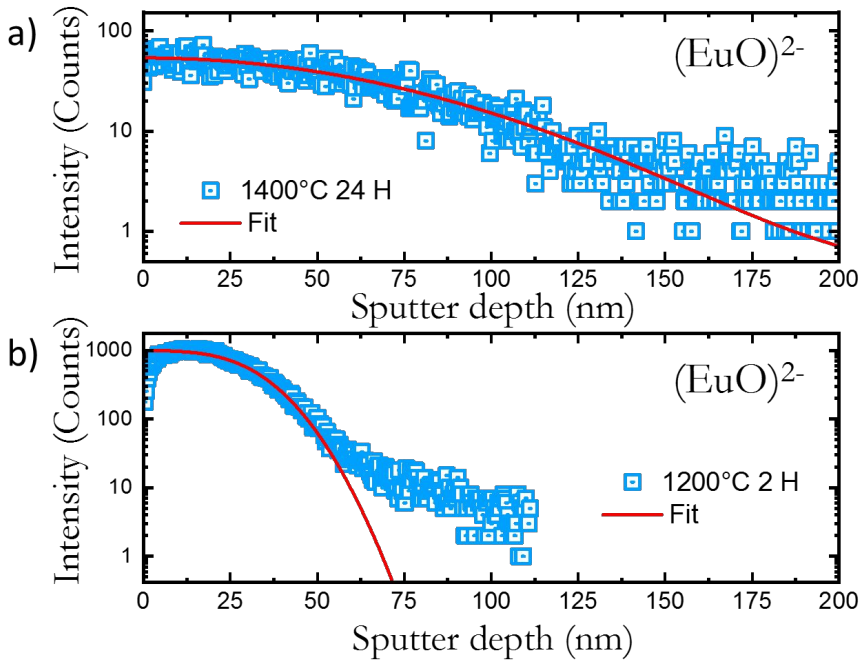

Figure 8: Higher resolution Eu-related TOF-SIMS signals of a thin ALD-grown Eu_2O_3 thin film on Y_2SiO_5 for annealing at 1400 °C for 2h (a) and 1200 °C for 24 h (b) respectively. Dots points are experimental data while solid lines are modelling using the diffusion equation (Eq. 1). One can note that a two-component contribution is visible for the 1200°C annealing sample.

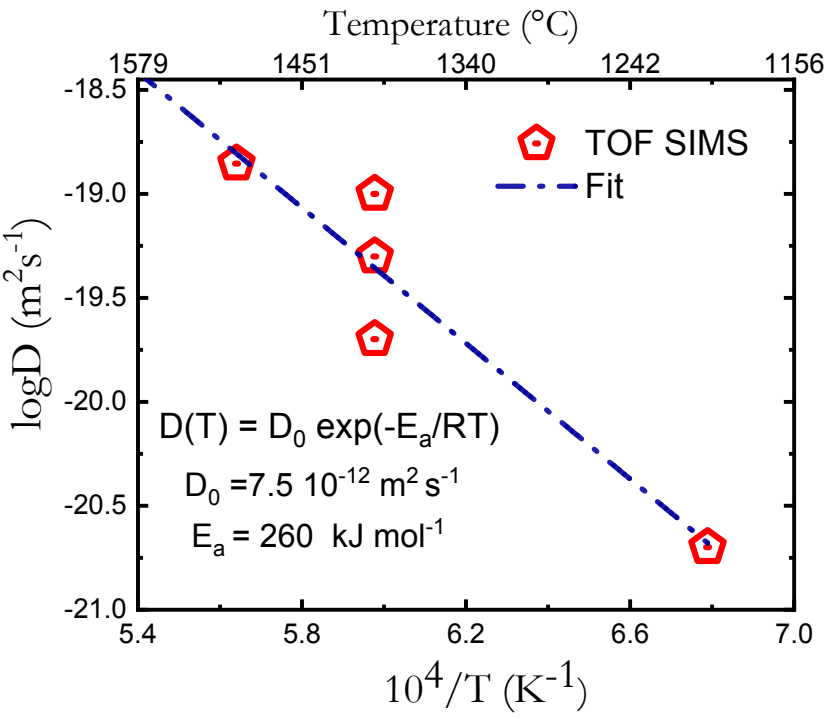

Figure 9: Arrhenius plot for Eu^{3+} diffusion in single crystal Y_2SiO_5 from TOF-SIMS measurements. The line is a least-squares fit of the data. Arrhenius parameters extracted from the fit are presented in the figure.

Table 2: Diffusion parameters and measured diffusion coefficients. Example from the literature have been added for comparison.

Crystal	Doping element	Annealing Temperature (°C)	Annealing Time (Hours)	D ($\times 10^{-20}$ m² s⁻¹)	Reference
Y_2SiO_5	Eu^{3+}	1200	2	0.2	This work

Y_2SiO_5	Eu^{3+}	1400	2	10	This work
Y_2SiO_5	Eu^{3+}	1400	10	5.0	This work
Y_2SiO_5	Eu^{3+}	1400	24	2.2	This work
Y_2SiO_5	Eu^{3+}	1500	2	13.4	This work
YVO4	Nd^{3+}	1400	24	78	[26]
$Y_3Al_5O_{12}$	Nd^{3+}	1200	25	0.26	[24]
$Y_3Al_5O_{12}$	Yb^{3+}	1450	24.1	4.3	[54,55]
Al_2O_3	Tr^{3+}	1200	48	3	[56]

3.3. Optical properties of in-diffused europium ions

Eventually, we evaluated the optical properties of Eu^{3+} ions diffused from the ALD layer into the YSO substrate. To this end, spectral hole burning (SHB) experiments were performed in fluorescence detection mode on a sample annealed for 90 h at 1400°C (More information available in the supporting information file). SHB is a highly sensitive technique used to probe the material's crystalline quality.[57,58] In this process, population is transferred from the ground state through the excited state of interest to a metastable states : the hyperfine levels (Figure S5). Indeed, dopant properties, such as optical

linewidth or nuclear spin lifetime, are strongly affected by crystal disorder (e.g. stacking fault, vacancies, mechanical strain, electric and magnetic noise). Moreover, the width of the spectral hole can provide information on the optical coherence lifetime since in the absence of power or laser broadening; it is expected to be twice the effective homogeneous linewidth. This linewidth is extremely sensitive to dynamical perturbation (moving charges, spin flip flop, two level systems) and act as an extremely sensitive strain and disorder probe and so SHB appears as a useful method to probe the surface.[57] We used several high intensity burning pulses at a given frequency to resonantly excite the Eu^{3+} ions into their $^5D_0$ state and create a corresponding transparency window in the inhomogeneously broadened absorption line (for more detail see Figure S4 and S5). Then after a delay of a few ms for the Eu^{3+} fluorescence to vanish, a subsequent weaker laser pulse (probe laser) was sent to the sample. This probe pulse was frequency swept across the burned hole frequency (-20 MHz, +20 MHz), with an acoustic optical modulator (AOM) to measure the excitation spectrum. Indeed in order to probe the pulse we worked in excitation mode by probing the change in the area of the red emission (i.e. the $^5D_0 \rightarrow {}^7F_2$ transition) as a function of the probe pulse wavelength. This change is due to the increased transparency at the hole frequency. First, we calibrated the experimental setup by burning a hole in a low Eu^{3+}-doped bulk Y_2SiO_5 single crystal (Figure S6). This measurement is useful in order to estimate the additional

broadening induced by the experimental conditions such as temperature, power broadening, laser linewidth and also laser stability. SHB signals recorded with this sequence present a hole FWHM of about 1.7 MHz (Figure S6). This value is broader than the best values reported for Eu^{3+}:YSO typically in the kHz range.[59–61] In our experiment an additional experimental broadening arises from the linewidth of our laser (300 kHz), the laser instability and the power broadening from this strongly focused configuration. SHB data was then recorded on the in-diffused sample (Fig. 10) for which the europium diffusion length ($2\sqrt{Dt}$) is estimated to 200 nm. To select the emission contribution originating from the in-diffused ions at the surface, we first aligned the setup in order to maximize the laser reflection at the surface. Then, a spectral hole was burned at the central frequency of 580.041 nm, from which, a promising hole linewidth as narrow as 4 MHz was obtained. This is about twice that of the low Eu^{3+} doped bulk reference sample. This difference is likely related to the higher Eu concentration at the surface (Figure 8). To discard any contribution trace Eu^{3+} ions in the YSO substrate also absorbing at the same central frequency, a second SHB experiment was performed at a slightly different wavelength of 580.057 nm, which is 15 GHz away from the central position of the inhomogeneous line. According to a study on an Eu^{3+}:YSO single crystal, the inhomogeneous linewidth is expected to linearly increase with Eu^{3+} concentration of about 21 GHz/%.[62] This concentration dependency suggest that the second SHB experiment are

perform on Eu^{3+} ions closer to the surface. At this wavelength a narrow hole can still be burned but with a larger FWHM (6 MHz) and shallower than the previous one. One possibility to explain the larger broadening in the diffused area compared to the reference, could be that an increase in concentration leads to some disorder in the structure that generates additional dynamical dephasing processes like Two Level System (TLS).[23] This disorder arises from possible variations of the local stoichiometry or interstitial defects since cation exchange occurs between two different material, Eu_2O_3 and Y_2SiO_5 respectively. More high-resolution spectroscopy measurements are required to determine the predominant dephasing mechanism. Anyway, this work demonstrates that RE ions can be spatially localized near the surface by a two-step process based on ALD deposition and annealing post treatment under appropriate conditions, while retaining their excellent optical properties. For various applications in quantum technologies, frequency-resolved optical pumping (i.e. spectral hole burning) appears as an essential preparation step. This step requires the possibility to address selectively by optical pumping each hyperfine sublevel. According to the hyperfine splitting of Eu^{63}, this implies that the spectral hole FWHM has to be narrower than 10 MHz. Therefore, an important issue of this work, is the demonstration of efficient burning of a sufficiently narrow hole for the in-diffused Eu:YSO. The measured FWHM of the burned hole is about 4.2 MHz, which remains suitable for the selective optical pumping. This

narrow FWHM suggests that Eu ions substitute to Y ions without significant distortion of the cation site as an important broadening of the hole would be expected in the case of disordered systems. For example, typical FWHM of SHB in Eu-doped silicate glasses are one order of magnitude broader, typically around 30-50 MHz.[64] Another relevant comparison may be done with thin films. Indeed, thin films constitute an alternative approach that could possibly allow one to benefit from the flexibility of multi-layers of variable thicknesses with spatially localized emitters. Currently, the only achievement of hole burning on films has been obtained on 3 μm-thick MOCVD-grown films of Eu:Y_2O_3 deposited on sapphire.[65] At the same temperature, the FWHM of the spectral hole was found to be significantly broader, around 30 MHz, indicating that crystalline quality of the film needs to be significantly improved before becoming an alternative to single crystal.

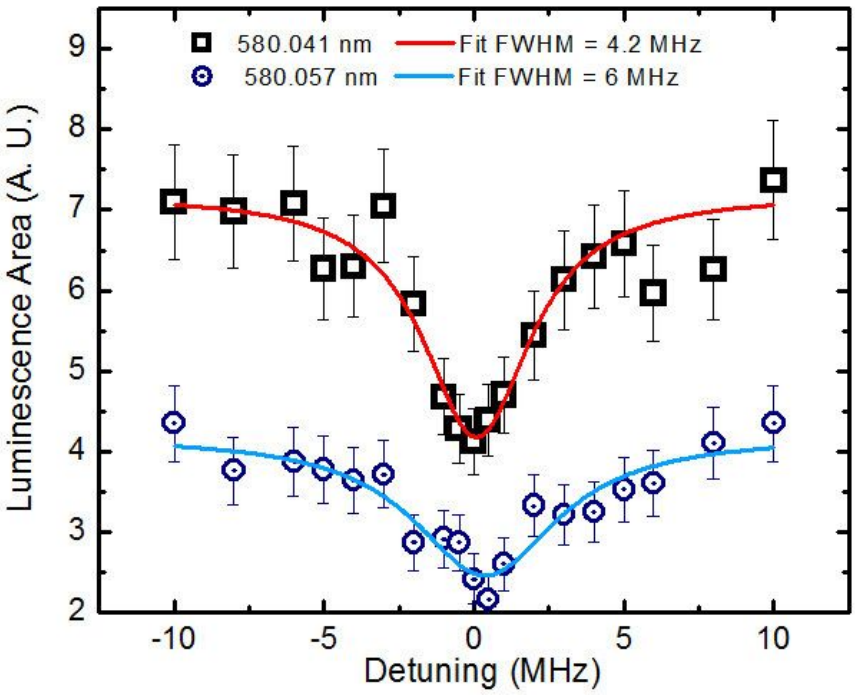

Figure 10. Fluorescence-detection of spectral holes burned on an ALD-Eu_2O_3 thin film on Y_2SiO_5 annealed 90 hours at 1400°C. Measurements at two different wavelengths of the inhomogeneous line are presented and the linewidth is given. Curves are vertically translated for better clarity.

Conclusion

In this work, we studied the ability of the ALD technique to spatially localize rare-earth ion emitters with good optical properties. In particular, we evaluated Eu^{3+} ion diffusion from few nanometers-thin Eu_2O_3 film grown by ALD into a polycrystalline Y_2O_3 film or into a single crystal Y_2SiO_5 substrate after thermal annealing in the 900-1400 °C range. While such high temperature post-treatments are essential to improve the crystallinity of thin ALD films, they lead to a partial

loss of RE ion localization. On the other hand, this behavior can be harnessed to locally diffuse emitters in the close proximity of the crystal surface.

Based on RBS and TOF-SIMS analyses, we observed that Eu^{3+} diffusion into polycrystalline Y_2O_3 becomes efficient at lower temperatures (900 °C) in comparison to single crystal YSO (1200 °C). This is attributed to the presence of grain boundaries that increase diffusion kinetics. Diffusion coefficients of about 4×10^{-21} and 2×10^{-20} $m^2.s^{-1}$ at 950°C and 1000 °C respectively in poly-Y_2O_3 and 2×10^{-21} and 10×10^{-20} $m^2.s^{-1}$ at 1200 and 1400 °C respectively were measured in a YSO single crystal.

This investigation indicates that, based on the nanometer-scale deposition ability of ALD associated with an appropriate thermal annealing, rare-earth oxide materials can be engineered with specific nanostructures in which dopant localization is well controlled. We eventually demonstrate that excellent optical properties are retained for such in-diffused near-surface RE ions in YSO. Spectral hole burning showed values as low as 4 MHz which could be improved by changing the composition of the top Eu_2O_3 layer that may lead to too high Eu^{3+} concentration close vicinity to the surface. This approach could provide an attractive alternative to rare-earth ion implantation and will be further explored in QTs applications such as quantum memories and

quantum sensors. Finally, this cation exchange method is versatile and can be applied to a large range of materials and doping elements (e.g. transition metal).

Supporting Information:

Detail on oxygen content measured by NRA; on the SiO_2 thickness measured by ellipsometry ; comparison of Eu diffusion profile deduced from TOF-SIMS and RBS; on the hole burning experimental setup; on energy level of Europium and on hole burning on Eu:Y_2SiO_5 single crystal.

Acknowledgements:

We acknowledge the French EMIR-A network for provision of irradiation beam time using the SAFIR facility and the financial support of the Paris network on quantum technologies (SIRTEQ), This project has received funding from the European Union Horizon 2020 research and innovation program under grant agreement no. 820391 (SQUARE) and no. 712721 (NANOQTECH).

References

(1) Goldner, P.; Ferrier, A.; Guillot-Noël, O. Rare Earth-Doped Crystals for Quantum Information Processing. In *Handbook on the Physics and Chemistry of Rare Earths*; Bünzli, J.-C. G., Pecharsky, V. K., Eds.; Elsevier, North Holland: Amsterdam, 2015; Vol. 46, pp 1–78.

(2) Korzenski, M. B.; Lecoeur, Ph.; Mercey, B.; Chippaux, D.; Raveau, B.; Desfeux, R. PLD-Grown Y_2O_3 Thin Films from Y Metal: An Advantageous Alternative to Films Deposited from Yttria. *Chem. Mater.* **2000**, *12* (10), 3139–3150. https://doi.org/10.1021/cm001094e.

(3) Singh, M. K.; Prakash, A.; Wolfowicz, G.; Wen, J.; Huang, Y.; Rajh, T.; Awschalom, D. D.; Zhong, T.; Guha, S. Epitaxial Er-Doped Y_2O_3 on Silicon for Quantum Coherent Devices. *APL Mater.* **2020**, *8* (3), 031111. https://doi.org/10.1063/1.5142611.

(4) Andriamiadamanana, C.; Ibanez, A.; Ferrier, A.; Joudrier, A.-L.; Lombez, L.; Liotaud, M.; Guillemoles, J.-F.; Pellé, F. Erbium-Doped Yttria Thin Films Prepared by Metal Organic Decomposition for up-Conversion. *Thin Solid Films* **2013**, *537*, 42–48. https://doi.org/10.1016/j.tsf.2013.04.093.

(5) Rubio, E. J.; Atuchin, V. V.; Kruchinin, V. N.; Pokrovsky, L. D.; Prosvirin, I. P.; Ramana, C. V. Electronic Structure and Optical Quality of Nanocrystalline Y_2O_3 Film Surfaces and Interfaces on Silicon. *J. Phys. Chem. C* **2014**, *118* (25), 13644–13651. https://doi.org/10.1021/jp502876r.

(6) Zhao, B.; Mattelaer, F.; Rampelberg, G.; Dendooven, J.; Detavernier, C. Thermal and Plasma-Enhanced Atomic Layer Deposition of Yttrium Oxide Films and the Properties of Water Wettability. *ACS Appl. Mater. Interfaces* **2020**, *12* (2), 3179–3187. https://doi.org/10.1021/acsami.9b18412.

(7) de Rouffignac, P.; Park, J.-S.; Gordon, R. G. Atomic Layer Deposition of Y_2O_3 Thin Films from Yttrium Tris(N,N'-Diisopropylacetamidinate) and Water. *Chem. Mater.* **2005,** 17, 4808-4814.

(8) Guo, H.; Zhang, W.; Lou, L.; Brioude, A.; Mugnier, J. Structure and Optical Properties of Rare Earth Doped Y_2O_3 Waveguide Films Derived by Sol–Gel Process. *Thin Solid Films* **2004**, *458* (1), 274–280. https://doi.org/10.1016/j.tsf.2003.12.059.

(9) Dibos, A. M.; Raha, M.; Phenicie, C. M.; Thompson, J. D. Atomic Source of Single Photons in the Telecom Band. *Phys. Rev. Lett.* **2018**, *120* (24), 243601. https://doi.org/10.1103/PhysRevLett.120.243601.

(10) Zhong, T.; Kindem, J. M.; Bartholomew, J. G.; Rochman, J.; Craiciu, I.; Miyazono, E.; Bettinelli, M.; Cavalli, E.; Verma, V.; Nam, S. W.; et al. Nanophotonic Rare-Earth Quantum Memory with Optically Controlled Retrieval. *Science* **2017**, *357* (6358), 1392–1395. https://doi.org/10.1126/science.aan5959.

(11) Tielrooij, K. J.; Orona, L.; Ferrier, A.; Badioli, M.; Navickaite, G.; Coop, S.; Nanot, S.; Kalinic, B.; Cesca, T.; Gaudreau, L.; et al. Electrical Control of Optical Emitter Relaxation Pathways Enabled by Graphene. *Nat. Phys.* **2015**, *11* (3), 281–287. https://doi.org/10.1038/nphys3204.

(12) Casabone, B.; Benedikter, J.; Hümmer, T.; Oehl, F.; Lima, K. de O.; Hänsch, T. W.; Ferrier, A.; Goldner, P.; Riedmatten, H. de; Hunger, D. Cavity-Enhanced Spectroscopy of a Few-Ion Ensemble in Eu^{3+} :Y_2O_3. *New J. Phys.* **2018**, *20* (9), 095006. https://doi.org/10.1088/1367-2630/aadf68.

(13) Wolf, T.; Neumann, P.; Nakamura, K.; Sumiya, H.; Ohshima, T.; Isoya, J.; Wrachtrup, J. Subpicotesla Diamond Magnetometry. *Phys. Rev. X* **2015**, *5* (4), 041001. https://doi.org/10.1103/PhysRevX.5.041001.

(14) Hoang, J.; Schwartz, R. N.; Wang, K. L.; Chang, J. P. Er^{3+} Interlayer Energy Migration as the Limiting Photoluminescence Quenching Factor in Nanostructured Er^{3+} :Y_2O_3 Thin Films. *J. Appl. Phys.* **2012**, *112* (2), 023116. https://doi.org/10.1063/1.4737793.

(15) Groot-Berning, K.; Kornher, T.; Jacob, G.; Stopp, F.; Dawkins, S. T.; Kolesov, R.; Wrachtrup, J.; Singer, K.; Schmidt-Kaler, F. Deterministic Single-Ion Implantation of Rare-Earth Ions for Nanometer-Resolution Color-Center Generation. *Phys. Rev. Lett.* **2019**, *123* (10), 106802. https://doi.org/10.1103/PhysRevLett.123.106802.

(16) van Dam, S. B.; Walsh, M.; Degen, M. J.; Bersin, E.; Mouradian, S. L.; Galiullin, A.; Ruf, M.; IJspeert, M.; Taminiau, T. H.; Hanson, R.; et al. Optical Coherence of Diamond Nitrogen-Vacancy Centers Formed by Ion Implantation and Annealing. *Phys. Rev. B* **2019**, *99* (16), 161203. https://doi.org/10.1103/PhysRevB.99.161203.

(17) Kukharchyk, N.; Shvarkov, S.; Probst, S.; Xia, K.; Becker, H.-W.; Pal, S.; Markmann, S.; Kolesov, R.; Siyushev, P.; Wrachtrup, J.; et al. Nanoscale Nonlinear Effects in Erbium-Implanted Yttrium Orthosilicate. *J. Lumin.* **2016**, *177*, 266–274. https://doi.org/10.1016/j.jlumin.2016.05.010.

(18) Kolesov, R.; Xia, K.; Reuter, R.; Stöhr, R.; Zappe, A.; Meijer, J.; Hemmer, P. R.; Wrachtrup, J. Optical Detection of a Single Rare-Earth Ion in a Crystal. *Nat. Commun.* **2012**, *3* (1), 1029. https://doi.org/10.1038/ncomms2034.

(19) Proslier, T.; Becker, N. G.; Pellin, M. J.; Klug, J.; Elam, J. W. Controlling the Emissive Properties of Materials-Improved Lasers and Upconversion Materials. US8518179B1, August 27, 2013.

(20) Rönn, J.; Karvonen, L.; Kauppinen, C.; Perros, A. P.; Peyghambarian, N.; Lipsanen, H.; Säynätjoki, A.; Sun, Z. Atomic Layer Engineering of Er-Ion Distribution in Highly Doped Er:Al_2O_3 for Photoluminescence Enhancement. *ACS Photonics* **2016**, *3* (11), 2040–2048. https://doi.org/10.1021/acsphotonics.6b00283.

(21) Scarafagio, M.; Tallaire, A.; Tielrooij, K.-J.; Cano, D.; Grishin, A.; Chavanne, M.-H.; Koppens, F. H. L.; Ringuedé, A.; Cassir, M.; Serrano, D.; et al. Ultrathin Eu- and Er-Doped Y_2O_3 Films with Optimized Optical Properties for Quantum Technologies. *J. Phys. Chem. C* **2019**, *123* (21), 13354–13364. https://doi.org/10.1021/acs.jpcc.9b02597.

(22) Welinski, S.; Thiel, C. W.; Dajczgewand, J.; Ferrier, A.; Cone, R. L.; Macfarlane, R. M.; Chanelière, T.; Louchet-Chauvet, A.; Goldner, P. Effects of Disorder on Optical and Electron Spin Linewidths in Er^{3+},Sc^{3+} :Y_2SiO_5. *Opt. Mater.* **2017**, *63*, 69–75. https://doi.org/10.1016/j.optmat.2016.09.039.

(23) Flinn, G. P.; Ganem, J.; Jones', M. L.; Meltzer, R. S.; Macfarlane, R. M. Sample Dependant Optical Dephasing in Bulk Crystalline Samles of Y_2O_3:Eu. *Phys. Rev. B* **1994**, *49*, 5821.

(24) Cherniak, D. J. Rare Earth Element and Gallium Diffusion in Yttrium Aluminum Garnet. *Phys. Chem. Miner.* **1998**, *26* (2), 156–163. https://doi.org/10.1007/s002690050172.

(25) Moya, E. G.; Moya, F.; Lesage, B.; LoudjanP, M. I.; Grattepainc, C. Yttrium Diffusion in A-Alumina Single Crystal. *J. Eur. Ceram.* **1998**, 18, 591-594.

(26) Hettrick, S. J.; Wilinson, S.; Sheperd, D. P. Neodymium and Gadolinium Diffusion in Yttrium Vanadate. *J. Opt. Soc. Am. B* **2002**, *19* (1), 33.

(27) Brady, J. B.; Cherniak, D. J. Diffusion in Minerals: An Overview of Published Experimental Diffusion Data. *Rev. Mineral. Geochem.* **2010**, *72* (1), 899–920. https://doi.org/10.2138/rmg.2010.72.20.

(28) Fujioka, K.; Sugiyama, A.; Fujimoto, Y.; Kawanaka, J.; Miyanaga, N. Ion Diffusion at the Bonding Interface of Undoped YAG/Yb:YAG Composite Ceramics. *Opt. Mater.* **2015**, *46*, 542–547. https://doi.org/10.1016/j.optmat.2015.05.023.

(29) Schmidt, R. V.; Kaminow, I. P. Metal-Diffused Optical Waveguides in $LiNbO_3$. *Appl. Phys. Lett.* **1974**, *25*, 458.

(30) Wang, T.-J.; Chen, B.-W.; Chen, P.-K.; Chen, C.-H. Er/Si Interdiffusion Effect on Photoluminescent Properties of Erbium Oxide/Silicon Oxide Films Deposited on Silicon. *J. Lumin.* **2017**, *192*, 1065–1071. https://doi.org/10.1016/j.jlumin.2017.08.050.

(31) Adachi, G.; Imanaka, N. The Binary Rare Earth Oxides. *Chem. Rev.* **1998**, *98* (4), 1479–1514. https://doi.org/10.1021/cr940055h.

(32) Ishibashi, H.; Shimomoto, K.; Nakahigashi, K. Electron Density Distribution and Chemical Bonding of Ln_2O_3 (Ln = Y, Tm, Yb) from Powder X-Ray Diffraction Data by the Maximum-Entropy Method. *J. Phys. Chem. Solids* **1994**, *55* (9), 809–814. https://doi.org/10.1016/0022-3697(94)90004-3.

(33) Ferrier, A.; Tumino, B.; Goldner, Ph. Variations in the Oscillator Strength of the $^7F_0 \rightarrow {}^5D_0$ Transition in Eu^{3+} : Y_2SiO_5 Single Crystals. *J. Lumin.* **2016**, *170*, 406–410. https://doi.org/10.1016/j.jlumin.2015.07.026.

(34) Denault, K. A.; Brgoch, J.; Kloß, S. D.; Gaultois, M. W.; Siewenie, J.; Page, K.; Seshadri, R. Average and Local Structure, Debye Temperature, and Structural Rigidity in Some Oxide Compounds Related to Phosphor Hosts. *ACS Appl. Mater. Interfaces* **2015**, *7* (13), 7264–7272. https://doi.org/10.1021/acsami.5b00445.

(35) Díaz, B.; Härkönen, E.; Światowska, J.; Maurice, V.; Seyeux, A.; Marcus, P.; Ritala, M. Low-Temperature Atomic Layer Deposition of Al_2O_3 Thin Coatings for Corrosion Protection of Steel: Surface and Electrochemical Analysis. *Corros. Sci.* **2011**, *53* (6), 2168–2175. https://doi.org/10.1016/j.corsci.2011.02.036.

(36) Härkönen, E.; Díaz, B.; Światowska, J.; Maurice, V.; Seyeux, A.; Vehkamäki, M.; Sajavaara, T.; Fenker, M.; Marcus, P.; Ritala, M. Corrosion Protection of Steel with Oxide Nanolaminates Grown by Atomic Layer Deposition. *J. Electrochem. Soc.* **2011**, *158* (11), C369. https://doi.org/10.1149/2.061111jes.

(37) Díaz, B.; Światowska, J.; Maurice, V.; Seyeux, A.; Normand, B.; Härkönen, E.; Ritala, M.; Marcus, P. Electrochemical and Time-of-Flight Secondary Ion Mass Spectrometry Analysis of Ultra-Thin Metal Oxide (Al_2O_3 and Ta_2O_5) Coatings Deposited by Atomic Layer Deposition on Stainless Steel. *Electrochimica Acta* **2011**, *56* (28), 10516–10523. https://doi.org/10.1016/j.electacta.2011.02.074.

(38) Potts, S. E.; Schmalz, L.; Fenker, M.; Díaz, B.; Światowska, J.; Maurice, V.; Seyeux, A.; Marcus, P.; Radnóczi, G.; Tóth, L.; et al. M. Ultra-Thin Aluminium Oxide Films Deposited by Plasma-Enhanced Atomic Layer Deposition for Corrosion Protection. *J. Electrochem. Soc.* **2011**, *158* (5), C132. https://doi.org/10.1149/1.3560197.

(39) Mayer, M. Improved Physics in SIMNRA 7. *Nucl. Instrum. Methods Phys. Res. Sect. B Beam Interact. Mater. At.* **2014**, *332*, 176–180. https://doi.org/10.1016/j.nimb.2014.02.056.

(40) Scarafagio, M.; Tallaire, A.; Chavanne, M.-H.; Cassir, M.; Ringuedé, A.; Serrano, D.; Goldner, P.; Ferrier, A. Improving the Luminescent Properties of Atomic Layer Deposition Eu:Y_2O_3 Thin Films through Optimized Thermal Annealing. *Phys. Status Solidi A* **2020**, 1900909. https://doi.org/10.1002/pssa.201900909.

(41) Shannon, R. D.; Prewitt, C. T. Effective Ionic Radii in Oxides and Fluorides. *Acta Crystallogr. B* **1969**, *25* (5), 925–946. https://doi.org/10.1107/S0567740869003220.

(42) Mehrer, H. *Diffusion in Solids : Fundamentals, Methods, Materials, Diffusion-Controlled Processes*; Springer series in Solid State Science; Springer-Verlag Berlin and Heidelberg GmbH & Co. K, 2009.

(43) Gaboriaud, R. J. Self-Diffusion of Yttrium in Monocrystalline Yttrium Oxide: Y_2O_3. *J. Solid State Chem.* 1980, pp 252–261.

(44) Zhou, B.; Shi, B.; Jin, D.; Liu, X. Controlling Upconversion Nanocrystals for Emerging Applications. *Nat. Nanotechnol.* **2015**, *10* (11), 924–936. https://doi.org/10.1038/nnano.2015.251.

(45) Wang, F.; Deng, R.; Wang, J.; Wang, Q.; Han, Y.; Zhu, H.; Chen, X.; Liu, X. Tuning Upconversion through Energy Migration in Core–Shell Nanoparticles. *Nat. Mater.* **2011**, *10* (12), 968–973. https://doi.org/10.1038/nmat3149.

(46) Wen, S.; Zhou, J.; Zheng, K.; Bednarkiewicz, A.; Liu, X.; Jin, D. Advances in Highly Doped Upconversion Nanoparticles. *Nat. Commun.* **2018**, *9* (1), 1–12. https://doi.org/10.1038/s41467-018-04813-5.

(47) Clausen, C.; Usmani, I.; Bussières, F.; Sangouard, N.; Afzelius, M.; Riedmatten, H. de; Gisin, N. Quantum Storage of Photonic Entanglement in a Crystal. *Nature* **2011**, *469* (7331), 508–511. https://doi.org/10.1038/nature09662.

(48) Bussières, F.; Clausen, C.; Tiranov, A.; Korzh, B.; Verma, V. B.; Nam, S. W.; Marsili, F.; Ferrier, A.; Goldner, P.; Herrmann, H.; et al. Quantum Teleportation from a Telecom-Wavelength Photon to a Solid-State Quantum Memory. *Nat. Photonics* **2014**, *8* (10), 775–778. https://doi.org/10.1038/nphoton.2014.215.

(49) Ortu, A.; Tiranov, A.; Welinski, S.; Fröwis, F.; Gisin, N.; Ferrier, A.; Goldner, P.; Afzelius, M. Simultaneous Coherence Enhancement of Optical and Microwave Transitions in Solid-State Electronic Spins. *Nat. Mater.* **2018**, *17* (8), 671–675. https://doi.org/10.1038/s41563-018-0138-x.

(50) Harrison, L. G. Influence of Dislocations on Diffusion Kinetics in Solids with Particular Reference to the Alkali Halides. *Trans. Faraday Soc.* **1961**, *57*, 1191. https://doi.org/10.1039/tf9615701191.

(51) Moya, E. G.; Moya, F.; Sami, A.; Juvé, D.; Tréheux, D.; Grattepain, C. Diffusion of Chromium in Alumina Single Crystals. *Philos. Mag. A* **1995**, *72* (4), 861–870. https://doi.org/10.1080/01418619508239939.

(52) Sabioni, A. C. S.; Huntz, A. M.; Daniel, A. M. J. M.; Macedo, W. A. A. Measurement of Iron Self-Diffusion in Hematite Single Crystals by Secondary Ion-Mass Spectrometry (SIMS) and Comparison with Cation Self-Diffusion in Corundum-Structure Oxides. *Philos. Mag.* **2005**, *85* (31), 3643–3658. https://doi.org/10.1080/14786430500323795.

(53) Carlson, W. D. Rates and Mechanism of Y, REE, and Cr Diffusion in Garnet. *Am. Mineral.* **2012**, *97* (10), 1598–1618. https://doi.org/10.2138/am.2012.4108.

(54) Marquardt, K.; Ramasse, Q. M.; Kisielowski, C.; Wirth, R. Diffusion in Yttrium Aluminium Garnet at the Nanometer-Scale: Insight into the Effective Grain Boundary Width. *Am. Mineral.* **2011**, *96* (10), 1521–1529. https://doi.org/10.2138/am.2011.3625.

(55) Marquardt, K.; Petrishcheva, E.; Abart, R.; Gardés, E.; Wirth, R.; Dohmen, R.; Becker, H.-W.; Heinrich, W. Volume Diffusion of Ytterbium in YAG: Thin-Film Experiments and Combined TEM–RBS Analysis. *Phys. Chem. Miner.* **2010**, *37* (10), 751–760. https://doi.org/10.1007/s00269-010-0373-4.

(56) Legros, C.; Lesage, B.; Borchardt, G.; Kilo, M.; Jomard, F. Lanthanide Diffusion in Single Crystalline and Polycrystalline Pure or Yttrium Doped Alpha-Alumina. *Defect Diffus. Forum* **2005**, *237–240*, 432–437. https://doi.org/10.4028/www.scientific.net/DDF.237-240.432.

(57) Bartholomew, J. G.; de Oliveira Lima, K.; Ferrier, A.; Goldner, P. Optical Line Width Broadening Mechanisms at the 10 KHz Level in Eu^{3+} :Y_2O_3 Nanoparticles. *Nano Lett.* **2017**, *17* (2), 778–787. https://doi.org/10.1021/acs.nanolett.6b03949.

(58) Lutz, T.; Veissier, L.; Thiel, C. W.; Woodburn, P. J. T.; Cone, R. L.; Barclay, P. E.; Tittel, W. Effects of Fabrication Methods on Spin Relaxation and Crystallite Quality in Tm-Doped $Y_3Al_5O_{12}$ Powders Studied Using Spectral Hole Burning. *Sci. Technol. Adv. Mater.* **2016**, *17* (1), 63–70. https://doi.org/10.1080/14686996.2016.1148528.

(59) Oswald, R.; Hansen, M. G.; Wiens, E.; Nevsky, A. Yu.; Schiller, S. Characteristics of Long-Lived Persistent Spectral Holes in Eu:Y_2SiO_5 at 1.2 K. *Phys. Rev. A* **2018**, *98* (6), 062516. https://doi.org/10.1103/PhysRevA.98.062516.

(60) Gobron, O.; Jung, K.; Galland, N.; Predehl, K.; Le Targat, R.; Ferrier, A.; Goldner, P.; Seidelin, S.; Le Coq, Y. Dispersive Heterodyne Probing Method for Laser Frequency Stabilization Based on Spectral Hole Burning in Rare-Earth Doped Crystals. *Opt. Express* **2017**, *25* (13), 15539. https://doi.org/10.1364/OE.25.015539.

(61) Zhang, S.; Galland, N.; Lučić, N.; Le Targat, R.; Ferrier, A.; Goldner, P.; Fang, B.; Le Coq, Y.; Seidelin, S. Inhomogeneous Response of an Ion Ensemble from Mechanical Stress. *Phys. Rev. Res.* **2020**, *2* (1), 013306. https://doi.org/10.1103/PhysRevResearch.2.013306.

(62) Könz, F.; Sun, Y.; Thiel, C. W.; Cone, R. L.; Equall, R. W.; Hutcheson, R. L.; Macfarlane, R. M. Temperature and Concentration Dependence of Optical Dephasing, Spectral-Hole Lifetime, and

Anisotropic Absorption in Eu^{3+}:Y_2SiO_5. *Phys. Rev. B* **2003**, *68* (8), 085109. https://doi.org/10.1103/PhysRevB.68.085109.

(63) Arcangeli, A.; Lovrić, M.; Tumino, B.; Ferrier, A.; Goldner, P. Spectroscopy and Coherence Lifetime Extension of Hyperfine Transitions in $^{151}Eu^{3+}$:Y_2SiO_5. *Phys. Rev. B* **2014**, *89* (18), 184305. https://doi.org/10.1103/PhysRevB.89.184305.

(64) MacFarlane, R. M.; Shelby, R. M. Homogeneous Line Broadening of Optical Transitions of Ions and Molecules in Glasses. *J. Lumin.* **1987**, *36* (4–5), 179–207. https://doi.org/10.1016/0022-2313(87)90194-3.

(65) Flinn, G. P.; Jang, K. W.; Ganem, J.; Jones, M. L.; Meltzer, R. S.; Macfarlane, R. M. Anomalous Optical Dephasing in Crystalline Y_2O_3: Eu^{3+}. *J. Lumin.* **1994**, *58* (1), 374–379. https://doi.org/10.1016/0022-2313(94)90441-3.

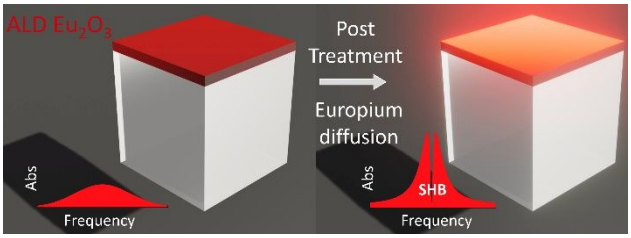
ALD Eu_2O_3
Post
Treatment
Europium
diffusion
Abs
Frequency
Abs
SHB
Frequency

TOC Graphic